Isospin dependence of intermediate mass fragment production in heavy-ion collisions at $E/A = 55$ MeV

J. F. Dempsey, R. J. Charity, and L. G. Sobotka
Department of Chemistry, Washington University, St. Louis, Missouri 63130

G. J. Kunde, S. Gaff, C. K. Gelbke, T. Glasmacher, M. J. Huang, R. C. Lemmon, W. G. Lynch, L. Manduci, L. Martin, and M. B. Tsang
Department of Physics and Astronomy and the National Superconducting Cyclotron Laboratory, Michigan State University, East Lansing, Michigan 48824

D. K. Agnihotri, B. Djerroud, W. U. Schröder, W. Skulski, and J. Tõke
Department of Chemistry and the Nuclear Structure Research Laboratory, University of Rochester, Rochester, New York 14627

W. A. Friedman
Department of Physics, University of Wisconsin, Madison, Wisconsin 53706
(Received 8 May 1996)

The production of intermediate mass fragments (IMF's) from the four reactions 55*A* MeV ^{124,136}Xe + ^{112,124}Sn is studied with an experimental apparatus which is highly efficient for the detection of both charged particles and neutrons. The IMF's are more localized in the midvelocity region than are the light charged particles, and the detected multiplicity of IMF's depends linearly on the charge lost from the projectile and increases with the neutron excess of the system. Remnants of the projectile, with very little velocity reduction, are found for most of the reaction cross section. Isotopic and isobaric fragment yields in the projectile-velocity region indicate that charge-to-mass ratio neutralization is generally not achieved but is approached when little remains of the projectile. For all systems, the fragments found in the midvelocity region are substantially more neutron rich than those found in the velocity region dominated by the emission from the projectile. This observation can be accounted for if the midvelocity source (or sources) is either more neutron rich or smaller, with the same neutron-to-proton ratio, than the source with the velocity of the projectile. Taken together, the observations of this work suggest that the intermediate mass fragments are, to a large extent, formed by multiple neck rupture of the overlap material, a process which might enhance the neutron-to-proton ratio of the primary source material and/or limit the size of the sources. This scenario is reminiscent of low-energy ternary fission and one predicted by Boltzmann-Uehling-Uhlenbeck calculations. However, these calculations predict too much velocity damping of the projectile remnant. The calculations improve, in this regard, when the in-medium nucleon-nucleon cross sections and the cost of creating low density material are reduced. [S0556-2813(96)02310-2]

PACS number(s): 25.70.Mn, 25.70.Lm, 25.70.Pq

I. INTRODUCTION

The copious production of intermediate mass fragments (IMF's), with mass intermediate between that characteristic of light particle evaporation and fission, is the distinguishing feature of intermediate-energy heavy-ion reactions [1]. The central question is, what does the production of these IMF's indicate? Several years ago a strong case was made that the production of IMF's indicated that the excited nuclear system expanded to the point that clusterization became probable [2]. The basis of this argument was that standard statistical models underpredicted the number of IMF's per light charged particle (LCP) while a statistical model which allowed for bulk expansion (and for subsequent compression, if the expansion energy was insufficient to totally fragment the system) could reproduce the IMF-to-LCP yield ratio [3]. More recently it has become clear that much of the IMF production in peripheral and midcentral collisions can be understood as multiple neck rupture, akin to what is believed to occur with low probability in low-energy fission [4,5]. This fragmentation scenario (which we do not distinguish from ''proximity fission'' [6]) occurs in solutions to the Boltzmann-Uehling-Uhlenbeck (BUU) equation [7,8], as well as scenarios, for central collisions, not found elsewhere in nuclear physics [9,10].

The multiple neck rupture scenario is made plausible by the observation that an overall binary reaction backbone exists for a large fraction of the reaction cross section at bombarding energies of several tens of MeV per nucleon bombarding energy, when both heavy projectiles and targets are involved [11–13]. There are two obvious differences between the original argument put forward to explain the IMF multiplicities and the multiple neck rupture scenario. The first is the dimensionality of the expansion and the second is the extent of the thermalization of the energy. Multiple neck rupture requires much less of the initial kinetic energy to be thermalized as the rupture process draws the energy needed to reduce the density directly from the relative kinetic energies of the reseparating fragments [14]. A third difference is that the second scenario allows for fragments to be produced

TABLE I. 55*A* MeV ^{124,136}Xe + ^{112,124}Sn.

Label	System	N/Z Projectile	N/Z Target	N/Z Total	$E_{\mathrm{c.m.}}$ (MeV)	$E_{\mathrm{c.m.}}/A$ (MeV)	$V_{\mathrm{c.m.}}$ (cm/ns)
LL	^{124}Xe + ^{112}Sn	1.30	1.24	1.27	3237	13.72	5.42
LH	^{124}Xe + ^{124}Sn	1.30	1.48	1.38	3410	13.75	5.15
HL	^{136}Xe + ^{112}Sn	1.52	1.24	1.38	3378	13.62	5.65
HH	^{136}Xe + ^{124}Sn	1.52	1.48	1.50	3567	13.72	5.39

from material which is ''surfacelike'' and thus perhaps neutron rich. Despite these significant differences, there are two features that these scenarios have in common. These are that the probability of producing detectable IMF's will depend on both the energetics of producing subsaturation nuclear material and the probability that the primary IMF's will survive the sequential decay process. Both of these issues depend on the charge-to-mass ratio of the reduced density nuclear material. The present work addresses these issues and tries to disentangle them from one another. Along with this we present and discuss the implications of many of the most prominent features of midcentral and peripheral collisions between heavy ions in the intermediate-energy region.

II. EXPERIMENT

This experiment was performed at the National Superconducting Cyclotron Laboratory at Michigan State University. The accelerator provided beams of 55*A* MeV ^{124}Xe and ^{136}Xe. Data were collected for each of these beams impinging on enriched (to 99%) targets of ^{112}Sn and ^{124}Sn, each of areal density 5.0 mg/cm^2. Some of the relevant numbers for these systems, and the abbreviations used throughout this work, are collected in Table I.

The detection of charged particles was provided at the most forward angles, 2.2°–4.5°, by an annular silicon strip detector [15] backed by an array of sixteen 2-cm-thick CsI(Tl) detectors. This forward telescope array (FA) provided unit charge resolution for $3<Z<56$ as well as excellent position information. In the present work, fragments with atomic numbers $Z>10$ detected in this telescope are called projectilelike fragments (PLF's). From 5.4° to 160.0°, light charged particles (LCP's, $Z\leqslant 2$) and intermediate mass fragments (IMF's, $Z\geqslant 3$) were detected in the Washington University/Michigan State University MINIWALL/BALL multidetector array [16]. These devices identify elements with $Z\leqslant 10$ and through varying angular regions, isotopes for $Z\leqslant 4$. The identification thresholds are 3*A* MeV except for *t* and ^{3}He for which the identification thresholds are 4*A* MeV.

The *Z*-dependent nonlinearities of the CsI(Tl) light output in the forward array were calibrated with beams of ^{136}Xe (at two energies), ^{84}Kr (two energies), ^{80}Kr (two energies), ^{68}Zn (two energies), ^{64}Zn (two energies), ^{60}Ni (two energies), ^{56}Fe (three energies), ^{52}Cr (three energies), ^{48}Ti (three energies), ^{18}O (three energies), and ^{12}C (one energy). A minimal set of calibration data for the MINIWALL/BALL was collected using elastic scattering of a 22.04*A* MeV molecular HeD beam (on ^{209}Bi) and from the punch through points for *p* and α particles. These data were then matched with the more extensive set compiled earlier [17], in which the *Z*-dependent nonlinearities of these devices had been determined.

The charged particle detection devices were placed inside the University of Rochester Superball neutron multiplicity meter [18]. Together these systems provide an unrivaled means to correlate the energy and charge of the projectile remnant, the charged particle emission characteristics, and the neutron multiplicity (N_n) with the total charge-to-mass ratio of the system and the asymmetry of this ratio between the target and projectile.

III. DATA

A. Gross trends of N_n, N_c, N_{lc}, and N_{IMF} subsection

Figure 1 shows the correlation between the number of detected charged particles (N_c) and the number of detected neutrons (N_n) for all four systems. The dependence of $\langle N_n\rangle$ along the ridges in these correlations is shown in Fig. 2. The correlations all exhibit the same general shape, the salient difference being an increase in $\langle N_n\rangle$ of about 6–12

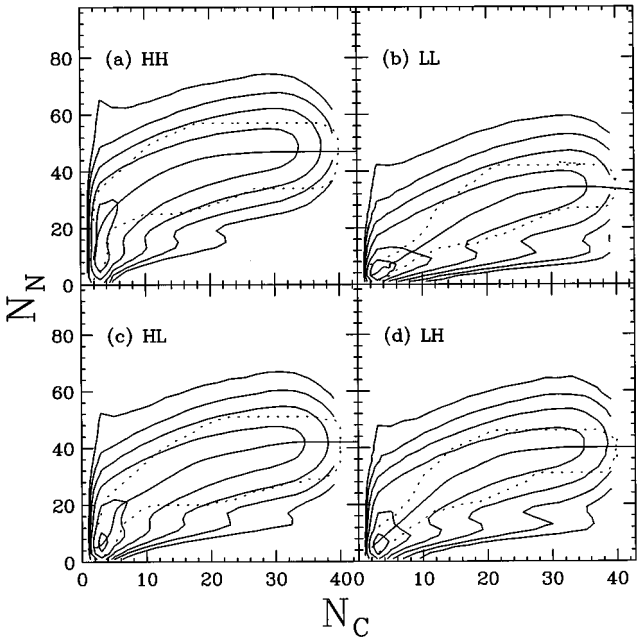

FIG. 1. Correlation between the number of detected charged particles (N_c) and the number of detected neutrons (N_n) for all four systems. The solid lines depict the ridges of the correlations (most probable value of N_n for each value of N_c). The dashed lines bracket the ridge and define the region used for generating mean values. The small second ridge at low values of N_n is due to instrumental effects.

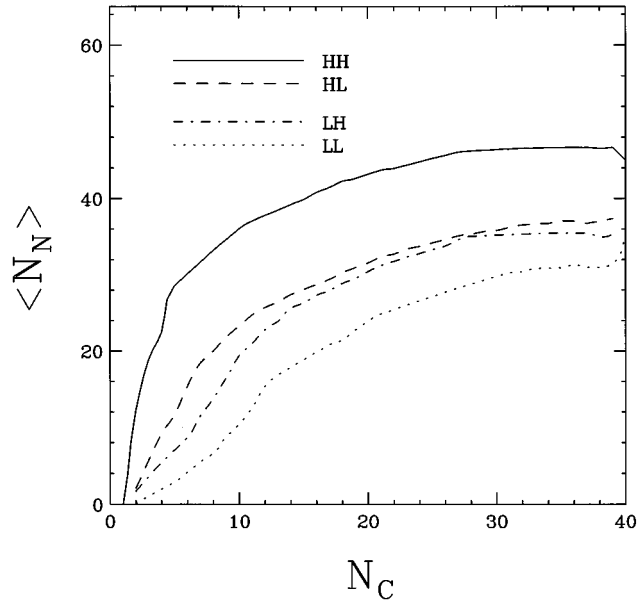

FIG. 2. Average value of N_n for each value of N_c for the four systems. The averages are calculated from the data inside the bracketed region (dotted lines) in Fig. 1. These data have been corrected for background but not efficiency.

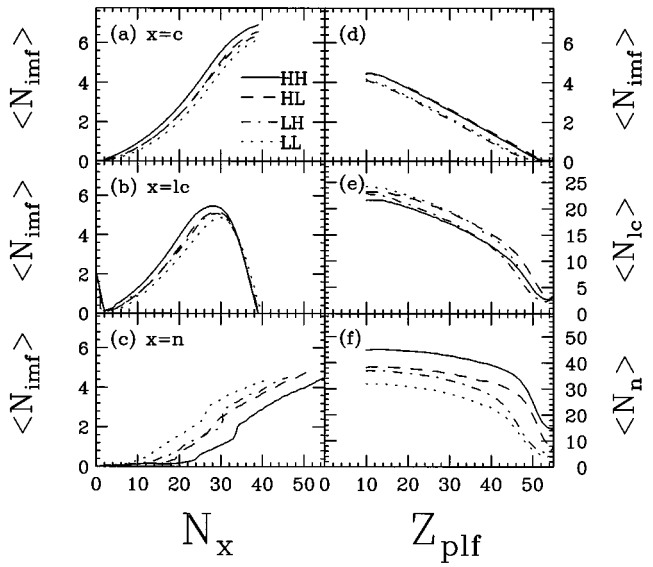

FIG. 3. The dependences of the average number of detected IMF's ($\langle N_{\rm IMF}\rangle$) on (a) the number of detected charged particles (N_c), (b) the number of detected light charged particles ($N_{\rm lc}$), and (c) the number of detected neutrons (N_n) are shown on the left-hand side. On the right-hand side, the dependences of (d) $N_{\rm IMF}$, (e) $N_{\rm lc}$, and (f) N_n on the charge of the projectilelike fragment ($Z_{\rm PLF}$) are shown. Each panel shows the dependences for all four systems. The same key is used throughout.

neutrons in going from the neutron-deficient projectile and target system LL to the mixed systems LH and HL, and another 6–12 neutron increase in going from these systems to the neutron-rich projectile and target system HH. Closer inspection of Fig. 2 shows that the offset in $\langle N_n\rangle$ is not constant with N_c. The maximum total offset, between LL and HH, occurs at moderately low values of $N_c\approx 10$ and reaches 22 neutrons, while for the upper half of the N_c distribution, the offset is only 12 units. It is more instructive to view the differences between these curves when horizontal shifts are applied to these data. For example the difference between the values of $\langle N_n\rangle$ for LL and HH is almost constant (at about 12 units) with N_c if the LL data are shifted on the abscissa by about 4–5 units. Our attempts to reproduce the dependence of $\langle N_n\rangle$ on N_c are discussed in Sec. IV along with the insight derived from this effort.

The dependences of the average number of detected IMF's ($\langle N_{\rm IMF}\rangle$) on the total detected number of charged particles (N_c), the number of detected light charged particles ($N_{\rm lc}$), and the number of detected neutrons (N_n) are shown in Figs. 3(a)–3(c), respectively, for all four systems. The values of $\langle N_{\rm IMF}\rangle$ increase with increasing N_c, $N_{\rm lc}$, and N_n, with the exception of the largest values of $N_{\rm lc}$ where charge conservation requires an anticorrelation. In addition to these trends, which are exhibited by all the systems, the values of $\langle N_{\rm IMF}\rangle$ increase with increasing neutron richness of the system for fixed values of N_c (a) and $N_{\rm lc}$ (b). On the other hand, $\langle N_{\rm IMF}\rangle$ decreases with increasing neutron richness of the system at fixed values of N_n (c). As was the case with Fig. 2, a more insightful way to view the curves shown on the left-hand side of Fig. 3 comes with the realization that the curves in each panel are almost identical to one another aside from a shift of the abscissa. The shifts are what one would expect if the ordinate $\langle N_{\rm IMF}\rangle$ was a measure of the total energy deposited and the abscissae represented various incomplete measures of this quantity. As an example, consider panel (b). For the HH system to emit as many light charged particles as the LL system more energy must be available for all emissions, because a larger fraction goes into neutron emission (in the HH as compared to the LL). The implication of this logic when applied to Fig. 2 is that, with the exception of the lowest values of N_c, the incremental neutron–to–charged-particle emission ratios are independent of system. In addition to these expected offsets, the left-hand side of Fig. 3 exhibits two other trends. The first of these is that the crossover systems LH and HL have very similar values of $N_{\rm IMF}$ which are intermediate to those found for the LL and HH systems. The second and more important observation is that the HH system (in any representation) has the largest *maximum* value of $N_{\rm IMF}$. The first additional point made just above is a rather trivial result of the close symmetry of the systems and the rather high efficiency of the apparatus for detection of IMF's emitted in the intermediate or midvelocity region ($V_\parallel\approx 0$ in the center-of-mass frame). The second point is significant in that it reflects, in great measure, the survivability of the produced IMF fragments and perhaps on the primary production probabilities. This point is discussed in Sec. IV.

B. Dependence of N_n, N_c, $N_{\rm lc}$, and $N_{\rm IMF}$ on the charge and energy of the projectile remnant

One of the most striking trends of these data is the dependence of $\langle N_{\rm IMF}\rangle$ on the charge of the projectile fragment $Z_{\rm IMF}$, detected in the FA. This is shown in Fig. 3(d). Here one sees that the number of detected IMF's increases by 1 for every 10 charges lost from the projectile. This rate is independent of the system; however, there is an offset which

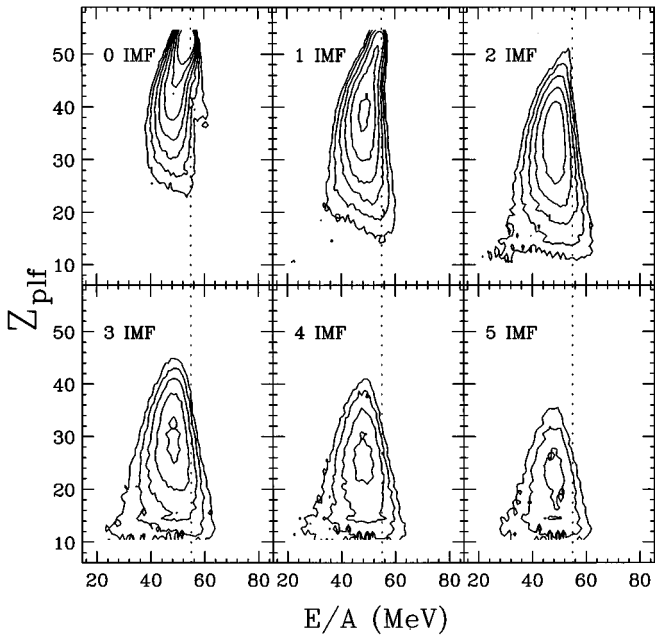

FIG. 4. Contour plots showing the variation of cross section with the the charge of the projectilelike fragment Z_{PLF} and the energy per nucleon E/A for different numbers of coincident intermediate mass fragments. The data from the LL system is displayed here. The dotted line is at 55 MeV/nucleon. The plots for the other systems look very similar.

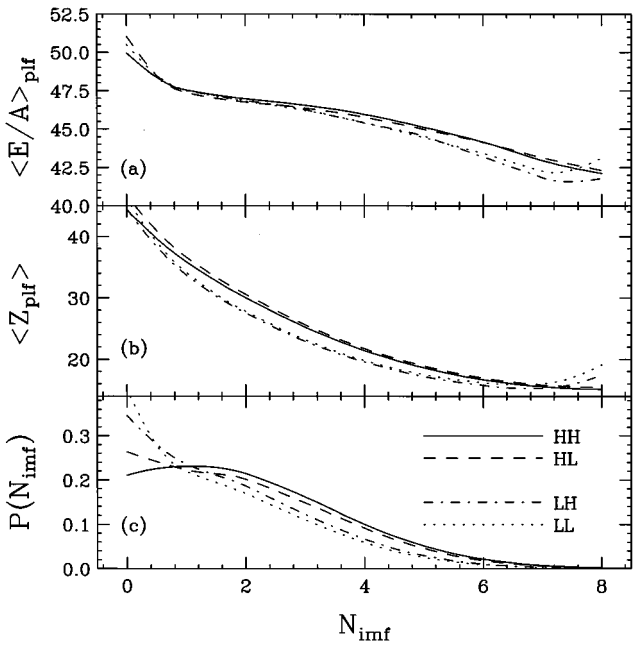

FIG. 5. The variation of $\langle E/A\rangle_{PLF}$ (a), $\langle Z_{PLF}\rangle$ (b), and the fractional yield or normalized probability of detecting a given number of IMF's (c) are shown as a function of the number of detected IMF's for all four systems.

depends *only* on the projectile. The systems with the neutron-rich projectile produce, on the average, 0.4 more intermediate mass fragments for the same charge loss or, alternatively, the systems with the neutron-deficient projectile must lose, on the average, 4 additional charge units before IMF production proceeds at the rate mentioned above. The bias imposed by the detection of a PLF ($Z>10$ detected in the FA) reduces the maximum value of $\langle N_{IMF}\rangle$ by about 2 units (1 if you count the detected PLF as an IMF). The lost fraction of the IMF distribution amounts to about 10% which corresponds to an upper limit of the lost cross section (upper limit because of the missed triggers for the most peripheral collisions) of about 0.4 b.

The other multiplicities N_{lc} [Fig. 3(e)] and N_n [Fig. 3(f)] are not as simply associated with Z_{PLF} and the projectile charge-to-mass ratio as is N_{IMF}. The trend in the values of N_{lc} show the necessarily complementary trend to that observed for N_{IMF}. Here, however, there is a kinematical bias for the largest values of Z_{PLF} which favors the HL system and suppresses the LH system. This bias is more evident for the LC particles than for IMF's because the former are much more characteristic of emission from the target and projectilelike fragments while the latter are more focused in the midvelocity region ($V_{\|}\approx 0$ in the center-of-mass frame); see Sec. III C.

The values of $\langle N_n\rangle$ evolve from ones which depend on the charge-to-mass ratio of the projectile when Z_{PLF} is near to that of the projectile to plateau values which depend on the total number of neutrons in the system for the smallest values of Z_{PLF}. The difference observed at large values of Z_{PLF} is due to the offset described above (the systems with the light projectile damp less energy to produce the same value of Z_{PLF}). The convergence of the HL and LH data sets, when Z_{PLF} gets very small, is expected from the approximate symmetry of the systems and the relatively high efficiency of the Superball for neutron detection from the center-of-mass frame which likely dominate the emissions in this limit. These data do not imply that charge-to-mass equilibration between the target and projectile is approached when Z_{PLF} is small. As we shall see later this equilibration process is incomplete even in this limit.

The influence of IMF production on the degree of velocity damping is shown in Fig. 4 for the LL system. The plots of the other systems are similar. In order to construct this plot we have used the post-evaporative mass relation given in [19]. These average masses should be accurate to within a few units except for charges near to the projectile, when the available energy is very small. However, for the LL system shown, this error should be less than 10%. As discussed above, there is the close tracking of the mean value of Z_{PLF} with the number of IMF's. In addition, these plots illustrate two other important features of these reactions. First, the extent of velocity damping is very small (at most 10% of the total relative velocity) and, second, the average damping is independent of the size of the remnant while the variation in damping grows with decreasing remnant size. The small degree of damping in slightly lower energy collisions of very heavy nuclei has been discussed before [11,13] and is a fundamental feature of these reactions which is not reproduced by mean field calculations. Here (at 55A MeV) the disagreement with model calculations also exists and is discussed in Sec. IV.

The important features mentioned above are collected in one-dimensional plots (using mean values) in Fig. 5. This figure illustrates that (a) the degree of damping is small and, to a very large extent, independent of system, (b) more

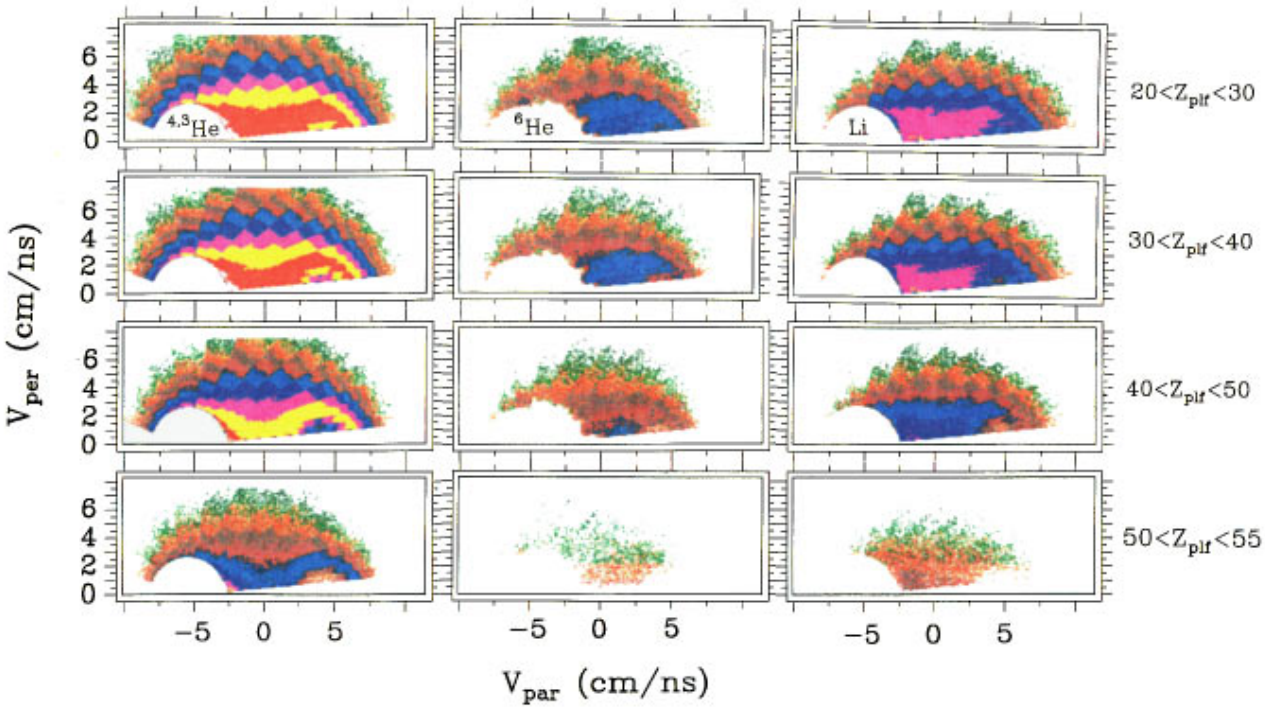

FIG. 6. Galilean-invariant cross section maps for α particles (left-hand side), ^{6}He fragments (center), and Li fragments (right-hand side) for four different gates on the charge of the projectile remnant, Z_{PLF} (as indicated), for the HH system. These plots are boosted into the center-of-mass system and use a logarithmic color scale. The projectile velocity is 5.0 cm/ns.

charge is lost per detected IMF when the projectile is neutron poor, and (c) overall, more IMF's are detected when the projectile is neutron rich.

C. Galilean-invariant cross section maps and azimuthal correlations

Figure 6 shows the Galilean-invariant cross section maps for α particles, ^{6}He, and Li fragments for four different gates on Z_{PLF} for the HH system. The velocity maps for α particles exhibit a strong projectilelike component, characterized by a ''Coulomb hole'' centered on the projectile velocity, when Z_{PLF} is large. The ''Coulomb hole'' resulting from targetlike emission is masked by the detection thresholds but part of the ridge is visible. While the prominence of this component fades with decreasing Z_{PLF}, it is always present and its center moves only slightly with Z_{PLF}. A quite different trend is seen for ^{6}He fragments which, independent of Z_{PLF}, exhibit an eccentric cross section distribution, peaked at the center of mass, stretched along the beam direction, and with almost no indication of a projectile ''Coulomb hole.''

To a very large extent the emission characteristics for Li are similar to those for ^{6}He. Here, however, there is more evidence for a projectile ''Coulomb hole'' (when $Z_{\mathrm{PLF}}>30$.) More interesting than the presence of this ''Coulomb hole'' is its asymmetry in the projectile frame. The backward portion is substantially more intense than the forward part. This emission pattern has been noticed in before [4,5] and is inconsistent with either emission from a single source at rest in the center of mass or sequential emission from targetlike and projectilelike sources.

The azimuthal correlations between the PLF and either LCP's or IMF's are peaked at 180° (see exceptions below). Examples of these correlations, cut on Z_{PLF} and $V_{\parallel}$, are shown for PLF-Li pairs in Fig. 7. The PLF-α and PLf-^{6}He correlations are similar to those shown. The 180° correlation increases in prominence as Z_{PLF} or $V_{\parallel}$ (of α particles, ^{6}He, Li, or other LCP's) increase. This correlation vanishes for Li when both the longitudinal velocity is small, $V_{\parallel}\approx 0$ cm/ns, and the value of Z_{PLF} is small (less than 25 or so).

Such correlations are expected for sequential decay, because the PLF angular distributions exhibit a steep angular dependence. This conventional explanation suits the PLF $-\alpha$-particle correlations. A similar explanation is likely to hold for the PLF-IMF correlations with the modification that the decay is not truly sequential.

All of the systems exhibit these same features and the maps gated on N_{IMF} are similar to those gated on Z_{PLF}. In the latter case (as was demonstrated previously) gating on progressively increasing values of N_{IMF} is equivalent to progressively decreasing values of Z_{PLF}.

D. Isotope ratios

The invariant cross section maps shown above illustrate that ^{6}He and ^{4}He have different emission patterns. The dependences of the ^{6}He/^{4,3}He ($R_{6/4}$) isotopic ratio and the ^{6}He/Li ($R_{6/\mathrm{Li}}$) and $t/^{3}$He ($R_{3/3}$) ''isobaric'' ratios on $V_{\parallel}$ and Z_{PLF} are shown in Figs. 8 and 9. Because of incomplete isotope resolution throughout the entire angular range, some isotopes have been mixed in order to create ratios in which we have confidence. Therefore the $R_{6/\mathrm{Li}}$ ratio, which uses all particle-bound Li isotopes, is only approximately isobaric. The variation of these ratios, which all have the yield of the more neutron-rich species in the numerator, with $V_{\parallel}$ and Z_{PLF} is among the most important experimental observations of this work.

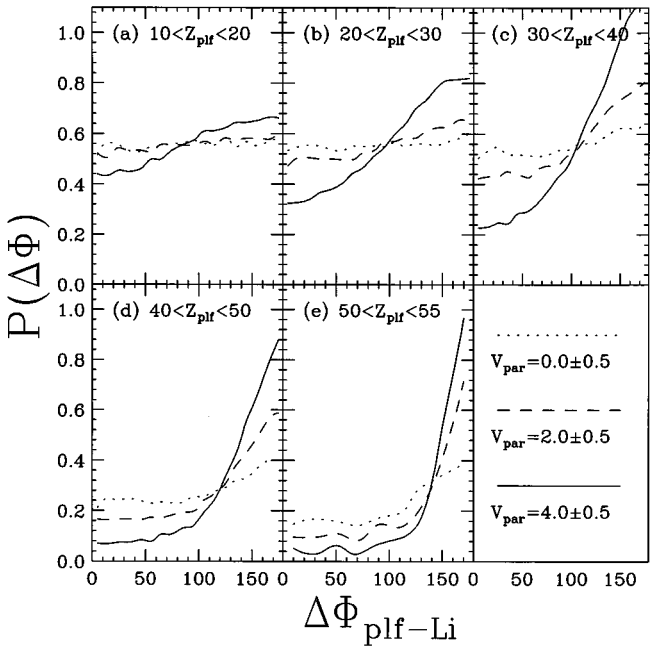

FIG. 7. Azimuthal distributions of Li fragments relative to the PLF's for five bins in Z_{PLF} and three cuts in $V_{\parallel}$ (in the c.m. system) for the HH system. Because the PLF's and the Li fragments are detected in different arrays (FA and MINIWALL/BALL, respectively), the detection method does not impose an autocorrelation. The angle $\Delta\Phi$ is defined relative to the PLF direction.

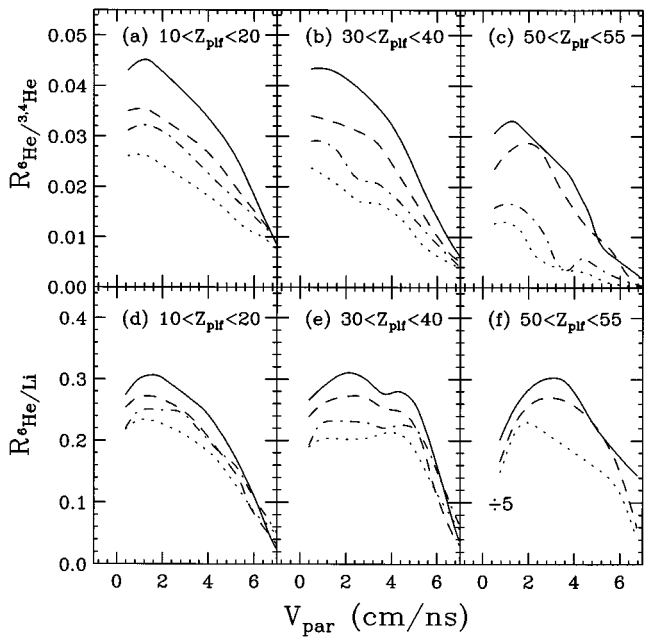

FIG. 8. The relative yields of ^{6}He to ^{3,4}He (a)–(c) and ^{6}He to Li (d)–(f) are shown as a function of $V_{\parallel}$ (in the c.m. system) for several gates on Z_{PLF}. The key for the lines is the same as that used in the previous figures. For clarity the data points themselves are suppressed. The statistical uncertainties are generally less than 5% with the exception of the LH system when Z_{PLF} is large, in which case the statistical uncertainties are (when these data are shown) less then 15%. The ratios in (f) have been multiplied by a factor of 5 for display purposes.

From these figures we note the following trends: (a) All ratios increase as the neutron excess of the system increases from LL to LH and HL to HH, (b) the fragments in the midvelocity region are more neutron rich than are the fragments in the projectile region, (c) the isotopic ratio decreases as the value of Z_{PLF} is increased while the isobaric ratios display the opposite trend, and (d) the diminution of the difference between the crossover systems (HL and LH) as the value of Z_{PLF} decreases (this is most clearly seen in the $R_{6/4}$ ratio).

The fact that the crossover systems approach, in the limit of very small values of Z_{PLF}, but never actually match each other, is expected based on the conclusion of studies of heavy-ion reactions just above the Coulomb barrier [20]. These lower-energy studies found that charge-to-mass equilibration does not occur sufficiently rapidly to be completed within the interaction time for a large fraction of the damped reaction cross section. The confirmation that charge-to-mass neutralization (neutralization is a less stringent condition than equilibration) does not generally occur in intermediate-energy heavy-ion reactions has been made prior to the present study by the work of Yennello *et al.* [21].

The trend with the value of Z_{PLF} mentioned above (c) is expected if the values of of Z_{PLF} are inversely related to the damped excitation energy. (As the excitation energy is increased the influence of the Coulomb barrier and separation energy are reduced; see below.) The observation that the fragments from the midvelocity region are more neutron rich than they are in the projectile-velocity region seems to suggest that the midvelocity source itself is more neutron rich than either the target or projectile sources. However, this is not the only possible explanation, a fact which becomes apparent in light of of statistical model calculations, a subject to which we now turn our attention.

IV. CALCULATIONS

A. Statistical model simulations

Figure 10 shows values of the ratios $R_{6/4}$, $R_{6/\mathrm{Li}}$, and $R_{3/3}$ calculated by GEMINI [22] and the expanding emitting source model (EES) [3]. The left-hand side of the figure [(a), (b), and (c)] shows the ratios as a function of the initial excitation energy per nucleon while the right-hand side [(d), (e), and (f)] shows the dependence on fragment size ($\eta = A_{\mathrm{source}}/A_{\mathrm{total}}$) with a fixed N/Z ratio. The N/Z ratio is taken to be that for the HH system.

Both codes treat the formation and sequential decay of all isotopes of H, He, Li, and Be. The sequential decay of all known narrow (less than 1 MeV) excited states of the isotopes of these elements is considered (either explicitly in the codes or their influence corrected for in a subsequent code). The results of these two codes agree with one another reasonably well and the calculated values of $R_{3/3}$ approach, but do not reach, the value expected for coalescence at the largest excitation energies. Despite this agreement, it would be a mistake to believe that these statistical expectations are robust in the accurate prediction of the yields of loosely bound particles. Our previous work on the statistical emission of *d*'s and *t*'s indicates that both direct reaction data and fusion data are needed to accurately calculate transmission coefficients [23]. Not surprisingly these calculations do not pro-

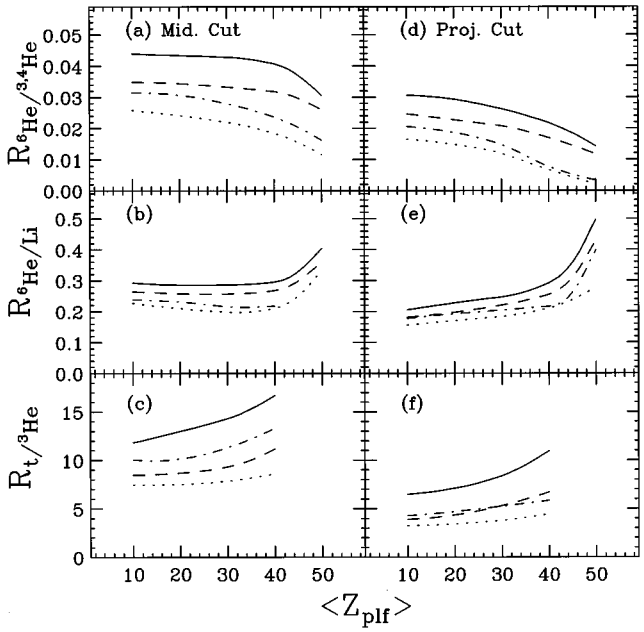

FIG. 9. The relative yield of ^{6}He to ^{3,4}He, ^{6}He to Li, and t to ^{3}He are shown for the four systems for several gates on Z_{PLF}. (a), (b), and (c) display the ratios for the midvelocity region, 0 cm/ns $< V_{\parallel}$(c.m.)$<$ 2.0 cm/ns, while (d), (e), and (f) display the ratios for the projectile region, 3.0 cm/ns $< V_{\parallel}$(c.m.)$<$ 7.0 cm/ns for (d) and (e) and 4 cm/ns for section (f). (The range had to be reduced for the last ratio due to the limitations imposed by the rather low t punch through energy.)

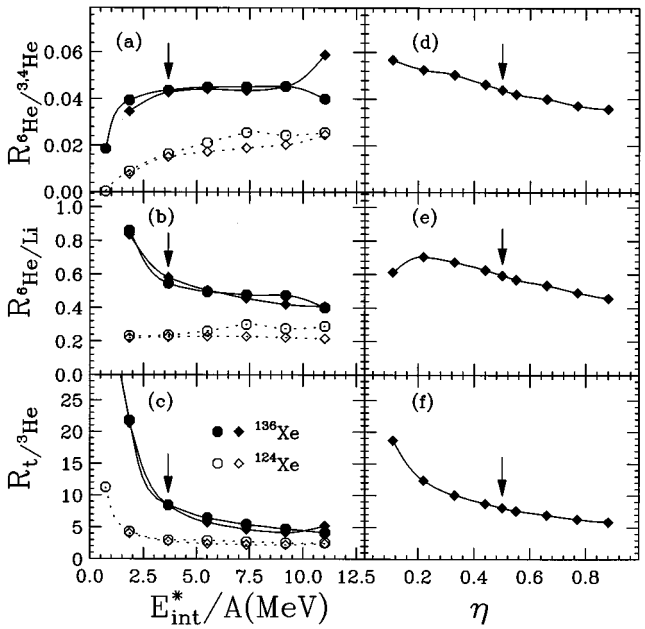

FIG. 10. The results of statistical model calculations for the decay of excited projectiles as a function of the initial excitation energy per nucleon [(a), (b), and (c)] and fragment size $\eta = A_{\mathrm{source}}/A_{\mathrm{total}}$ at fixed charge-to-mass ratio [(d), (e), and (f)]. In the latter case, the charge-to-mass ratio is that of the H projectile, ^{136}Xe, and the initial excitation energy per nucleon is 3.68 (arrow on left.) The circles are the results from GEMINI calculations and the diamonds are the results from the EES. The key for the lines is the same as that used in the previous figures.

vide a quantitative explanation of the experimental data presented in the previous section. On the other hand, the calculations do account for the trends seen in the data and, in doing so, provide considerable insight into the sources of these fragments.

As expected, the calculated trend of the isotopic ratio with excitation energy is opposite to that of the isobaric ratios. The explanation of both trends is that offered above—the barrier or separation energy determines the yield at low excitation energy and the influence of these quantities diminishes as the excitation energy is increased. The observed trends with Z_{PLF} are then readily explained as long as one accepts that the thermalized energy increases as the value Z_{PLF} decreases, a reasonable contention supported by the fragment multiplicities (see Fig. 3.)

Less obvious than the explanation of the trends with Z_{PLF} is the explanation for the observed increase in the yield of neutron-rich fragments as $V_{\parallel}$ is decreased from the projectile region to that of the center of mass. This observation has been made previously for the isotopes of H [5] and is reminiscent of the charged particles which accompany low-energy fission [24]. (We remind the reader that after α particles, t's are the most prevalent light charged particle which accompanies fission.)

If one tries to explain the observed trends utilizing sources of the same size and charge-to-mass ratios in the midvelocity and projectile-velocity regions, then the isobaric ratios imply that the midvelocity source has a lower excitation energy per nucleon than the projectilelike source. This explanation is inconsistent with all reaction models and with the kinetic ''temperatures'' (extracted from the transverse energy spectra) which are large (in the range of 20 MeV) and, what is more important, larger in the midvelocity region than in the region of velocity around that of the projectile.

Two possibilities remain to explain these observations. The first, and obvious one, is that the isotope ratios in the midvelocity region are enriched in neutron-rich isotopes because the source material is neutron rich relative to the bulk matter which should be represented by the emissions in the projectile region (in either the HH or LL systems). A second possibility is investigated on the left-hand side of Fig. 10, which displays EES predictions for the various ratios under study as a function of $\eta = A_{\mathrm{source}}/A_{\mathrm{total}}$, for the charge-to-mass ratio of the HH system. The ratios increase as η decreases, thus providing an argument that the midvelocity sources can have the same charge-to-mass ratio as the overall system as long as these sources are always smaller than the source in the projectile-velocity region. In this case the midvelocity sources are not neutron rich relative to the bulk matter but they are neutron rich relative to the valley of β stability. Needless to say, this case argues against a single large midvelocity source (as do the Galilean-invariant plots).

A more elementary testing ground for model calculations than these isotopic and isobaric ratios are the values of N_n/N_c as a function of Z_{PLF} or the dependence of $\langle N_n \rangle$ on N_c as shown in Fig. 2. We have done statistical calculations assuming three source regions (with the target, c.m., and projectile velocities) in which we have fixed the total mass in each region by partitioning the mass of the total system as indicated by the Galilean-invariant cross section maps. These

calculations were corrected for both the neutron tank efficiency and MINIWALL/BALL thresholds.

These calculations reproduce the general trend of $\langle N_n \rangle$ with N_c (with both values increasing with increasing excitation energy per nucleon); however, the results are sensitive to the prescription for the level density constant a and the number of sources in each region. Including the variation of these quantities, the exercise of reproducing the dependence of $\langle N_n \rangle$ on N_c is underdetermined. For example using a small or temperature-dependent prescription for a suppresses n emission and enhances the production of particles with large separation energies. Variation of a within a reasonable range (from $A/8$ to the smooth temperature dependent prescription suggested by Ormand *et al.* [25]) reduces the neutron yield by about 20%. Furthermore, decreasing the source size (from $\eta = 1$ to 0.25), and thus increasing the number of sources, increases the $\langle N_n \rangle$-to-N_c ratio (for the same reason that the isotope and isobaric ratios increased with decreasing η). These calculations indicate that while there is not a unique prescription to reproduce the experimental data, multiple sources are needed to produce enough free neutrons if the level density parameter a is either small ($A/11$) or temperature dependent [25].

These statistical model calculations can also be used to investigate the significance of the observation made in the previous section that the maximum values of $\langle N_{\mathrm{IMF}} \rangle$ increase with neutron excess. This might very well be only the result of the improved survivability (retention of IMF status) of the more neutron-rich primary fragments which will result from the sequential decay of the neutron-rich systems. However, if the differential survivability cannot explain the entire difference, it is possible that this difference, in some measure, reflects the relative ease of density reduction in matter of different charge-to-mass ratios.

To address this issue we calculated the IMF ''survivability'' (percentage of produced IMF's which retain their IMF status, $Z>2$, after sequential decay) with the statistical model codes. The results from the EES using a single source (of the size of the projectile) are presented in Fig. 11. (The production and sequential decay of elements with $Z \geq 5$ are treated in less detail than those with $Z<5$; however, with increasing Z and A the survivability, retention of IMF status, is quite high. This fact, coupled with the decreasing yield with increasing Z_{IMF} makes the detailed treatment of the heavier fragments not relevant to the survivability question.) In this representative calculation the difference in the surviving fraction (long dashed line) is predicted to be in the range of 30% – 10% of the total fraction of surviving IMF's. This is a substantial difference, not dissimilar to the difference in the data, and thus we must conclude that most, if not all, of the observed difference results from the action of sequential decay.

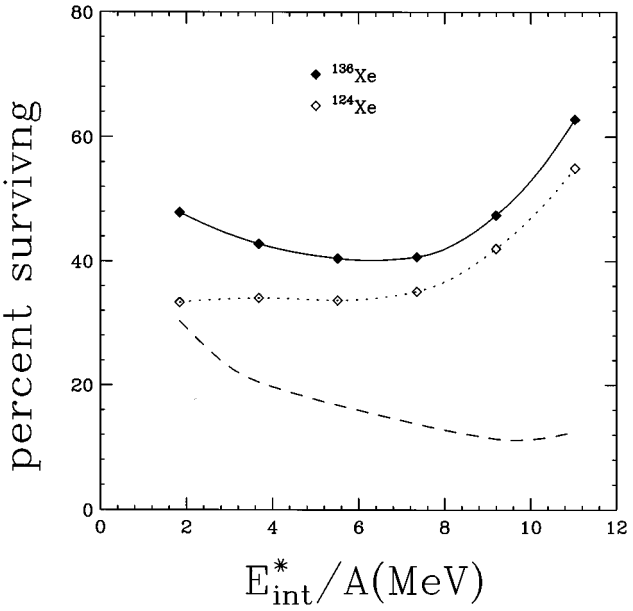

FIG. 11. Statistical model predictions (EES) of the percentage of IMF's which survive sequential decay and retain their IMF status. The dashed line is the percentage difference in the survivability.

B. Dynamical reaction simulations

Many of the observations made above provide a qualitative argument for a reaction picture which produces a string of small emitters with intermediate velocities. Both TDHF calculations [26] and macroscopic dynamical models [27] can produce fragments from the ''neck'' region; however, more appropriate to the energy region of the present study are Boltzmann-Uehling-Uhlenbeck (BUU) reaction simulations, in which the effects of two-body collisions are taken into account. These simulations are also known to produce intermediate velocity (''necklike'') sources [7]. We have therefore preformed BUU simulations [28] for the systems studied in the present work. Some of the results of these calculations are shown in Fig. 12. The striking feature of these calculations, in comparison to the experimental data, is the overprediction of the velocity damping; compare Fig. 12(a) with Fig. 5(a). The data have a negligible cross section (less than 100 mb) with values of E/A less than 40 MeV while the calculations predict large cross sections (as much as 1 b) in this energy region. This discrepancy is largest if a stiff equation of state is used (incompressibility $K=380$), smaller with a soft equation of state (incompressibility $K=200$), and still smaller if the isospin degree of freedom is modeled in a fashion which allows for stable neutron skins (isospin soft) [8]. The decreased damping (in going from stiff to soft for example) is accompanied by an increase in the mass contained in fragments with velocities intermediate between the projectile and the target (the midvelocity range), Fig. 12(b). (It is also accompanied by a general increase in the multiplicity of fragments from the neck region. We choose not to display this trend because this fragmentation has much to do with the numerical implementation of the BUU equation.) Therefore we conclude that calculations of this sort (BUU simulations without fluctuations) come closer to reproducing the experimental data when the cost of creating reduced density material is reduced. (This holds for soft versus stiff and isospin soft versus soft.) Reduction in the velocity damping can also be accomplished by reducing the nucleon-nucleon cross section. However, even with a density-dependent reduction which reduces the cross sections by 20% at the saturation density [29] and the isospin-dependent soft equation of state, the damping is still excessive; see Fig. 12. (A further decrease in the nucleon-nucleon

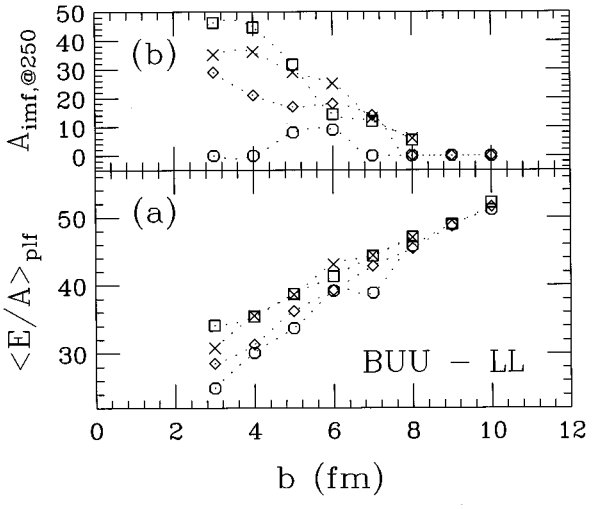

FIG. 12. The results of BUU calculations for (a) the exit channel value of E/A for the projectilelike fragment and (b) the mass contained in midvelocity IMF's at 250 fm/c. The circles show the results for a stiff ($K=380$ MeV) equation of state, the diamonds show the results for a soft ($K=200$ MeV) equation of state, the $\times$'s show the results for the iso-soft equation of state which has an improved treatment of the isospin degree of freedom, and the squares show the results for the iso-soft equation of state when the scattering cross sections have a density-dependent reduction.

cross sections would further diminish this discrepancy. Unfortunately, the meaning of these cross sections is unclear since the BUU simulations do not treat medium modifications in a self-consistent fashion.) Perhaps more germane than the equation of state or the in-medium cross section is the neglect of fluctuations in these simulations. It is possible that the failure cited above results from this omission, a possibility which must be tested with improved models.

We have verified that momentum-dependent potentials have little affect on the observables presented above at the energy of the present study. Furthermore, we would like to mention that we have chosen to display and compare the results for the LL system because the mass uncertainty for experimental data is smallest here. We also hasten to point out that if the experimental masses (for a given charge) are less than assumed [19], then the experimental E/A values would be even larger (implying even less velocity dissipation) than those shown in Fig. 5(a).

V. SUMMARY

The present work examines a set of systems, ^{124,136}Xe + ^{112,124}Sn at 55A MeV, which allowed for a study of the influence of the charge-to-mass ratio on the neutron and charged particle emission characteristics. Our experimental results were compared to both statistical and dynamical simulations of these reactions. The detected multiplicity of intermediate mass fragments increases with the neutron excess of the system. This result is counter to the expectation based on general fissility arguments but is understandable in light of sequential decay considerations. The isotopic and isobaric ratios of the emitted fragments indicate that the fragments formed in the intermediate velocity region either arise from material which is more neutron rich than is the average matter or that the primary sources in the intermediate velocity region are small and neutron rich relative to stable nuclei. The latter would be the case if the intermediate sources were much smaller than the target and projectile, yet had the charge-to-mass ratio of the target and projectile. In either case, these results are consistent with a participant-spectator model; however, in one case the participant region is enriched in neutron-rich, perhaps surfacelike, material, and in the other the participant region is never a single source.

This result is consistent with the gross picture presented by BUU calculations; however, these calculations overpredict the extent of velocity damping in these collisions. Softening the equation of state, providing an improved isospin treatment, and reducing the nucleon-nucleon scattering cross sections lessen this disagreement while at the same time increasing the mass in bound fragments in the neck or midvelocity region at the end of the collisions, which is the telltale feature of these reactions.

ACKNOWLEDGMENTS

One of us (G.J.K.) acknowledges support by the Alexander von Humboldt foundation. This work was supported by the U.S. Department of Energy under Grant Nos. DE-FG02-87ER40316 (Washington University) and DE-FG02-88ER40414 (University of Rochester), and by the National Science Foundation under Grant Nos. PHY-92-14992, PHY-95-28844 (NSCL), and PHY-93-14131 (University of Wisconsin, Nuclear Theory).

[1] L.G. Moretto and G.J. Wozniak, Annu. Rev. Nucl. Part. Sci. **43**, 379 (1993).

[2] D.R. Bowman, C.M. Mader, G.F. Peaslee, W. Bauer, N. Carlin, R.T. de Souza, C.K. Gelbke, W.G. Gong, Y.D. Kim, M.A. Lisa, W.G. Lynch, L. Phair, M.B. Tsang, C. Williams, N. Colonna, K. Hanold, M.A. McMahan, G.J. Wozniak, L.G. Moretto, and W.A. Friedman, Phys. Rev. C **46**, 1834 (1992).

[3] W.A. Friedman, Phys. Rev. Lett. **60**, 2125 (1988); Phys. Rev. C **42**, 667 (1990).

[4] C.P. Montoya, W.G. Lynch, D.R. Bowman, G.F. Peaslee, N. Carlin, R.T. de Souza, C.K. Gelbke, W.G. Gong, Y.D. Kim, M.A. Lisa, L. Phair, M.B. Tsang, J.B. Webster, C. Williams, N. Colonna, K. Hanold, M.A. McMahan, G.J. Wozniak, and L.G. Moretto, Phys. Rev. Lett. **73**, 3070 (1994).

[5] J. Tõke, B. Lott, S.P. Baldwin, B.M. Quednau, W.U. Schröder, L.G. Sobotka, J. Barreto, R.J. Charity, D.G. Sarantites, D.W. Stracener, and R.T. de Souza, Phys. Rev. Lett. **75**, 2920 (1995).

[6] A.A. Stefanini, C. Casini, P.R. Maurenzig, A. Olmi, R.J. Charity, R. Freifelder, A. Gobbi, N. Herrmann, K.D. Hildenbrand, M. Petrovici, F. Rami, H. Stelzer, J.P. Wessels, M. Gnirs, D. Pelte, J. Galin, D. Guerreau, U. Jahnke, A. Péghaire, J.C. Ad-

loff, B. Bilwes, R. Bilwes, and G. Rudolf, Z. Phys. A **351**, 167 (1995).

[7] M.B. Tsang, G.F. Bertsch, W.G. Lynch, and M. Tohyama, Phys. Rev. C **40**, 1685 (1989).

[8] L.G. Sobotka, Phys. Rev. C **50**, R1272 (1994).

[9] L.G. Moretto, K. Tso, N. Colonna, and G.J. Wozniak, Phys. Rev. Lett. **69**, 1884 (1992).

[10] W. Bauer, G.F. Bertsch, and H. Schulz, Phys. Rev. Lett. **69**, 1888 (1992).

[11] B. Lott, S.P. Baldwin, B.M. Szabo, B.M. Quednau, W.U. Schröder, J. Tõke, L.G. Sobotka, J. Barreto, R.J. Charity, L. Gallamore, D.G. Sarantites, D.W. Stracener, and R.T. de Souza, Phys. Rev. Lett. **68**, 3141 (1992).

[12] J.F. Lecolley, L. Stuttgé, M. Aboufirassi, A. Badala, B. Bilwes, R. Bougault, R. Brou, F. Cosmo, J. Colin, D. Durand, J. Galin, A. Genoux-Lubain, D. Guerreau, D. Horn, D. Jacquet, J.L. Laville, F. Lefebvres, C. Le Brun, J. Lemière, O. Lopez, M. Louvel, M. Mahi, M. Morjean, C. Paulot, A. Péghaire, N. Prot, G. Rudolf, F. Scheibling, J.C. Steckmeyer, B. Tamain, and S. Tomasevic, Phys. Lett. B **325**, 317 (1994).

[13] S.P. Baldwin, B. Lott, B.M. Szabo, B.M. Quednau, W.U. Schröder, J. Tõke, L.G. Sobotka, J. Barreto, R.J. Charity, L. Gallamore, D.G. Sarantites, D.W. Stracener, and R.T. de Souza, Phys. Rev. Lett. **74**, 1299 (1995).

[14] J. Tõke, D.K. Agnihotri, S.P. Baldwin, B. Djerroud, B. Lott, B.M. Quednau, W. Skulski, W.U. Schröder, L.G. Sobotka, R.J. Charity, D.G. Sarantites, and R.T. de Souza (submitted).

[15] Design S from Micron Semiconductor, 1 Royal Buildings, Marlorough Road, Churchill Industrial Estate, Lancing, Sussex BN15 8UN, England. This device is sectioned into 4 sets of 16 radial strips each and 16 azimuthal (pie shaped) sectors.

[16] The MINIWALL is comprised of 112 fast plastic-CsI(Tl) phoswich detectors spanning 5.4° to 25.0°. The logic and electronics is similar to that used for the the Dwarf Ball: D.W. Stracener, *et al.* Nucl. Instrum. Methods A **294**, 485 (1990). The MINIBALL, which mates to the MINIWALL at 25.0° and extends back to 160°, works with the same type detector elements and is fully described in R.T. deSouza *et al.*, ibid. **295**, 109 (1990).

[17] R.J. Charity, L.G. Sobotka, N.J. Robertson, D.G. Sarantites, J. Dinius, C.K. Gelbke, T. Glasmacher, D.O. Handzy, W.C. Hsi, M.J. Huang, W.G. Lynch, C.P. Monotoya, G.F. Peaslee, C. Schwarz, and M.B. Tsang, Phys. Rev. C **52**, 3126 (1995).

[18] This device consists of 16.3 m^3 of Gd-loaded liquid scintillator viewed by 52 5″ photomultiplier tubes. The device provides a prompt signal from the initial *n-p* interactions, and subsequent signals when each of the neutrons is captured. Crude estimates of the efficiencies for neutron detection from projectile, target, and center-of-mass sources are approximately 33%, 78%, and 80%, respectively. The Superball is described in detail in W.U. Schröder, University of Rochester Report No. DOE-ER-79048-1, 1995.

[19] R.J. Charity, D.R. Bowman, Z.H. Liu, R.J. McDonald, M.A. McMahan, G.J. Wozniak, L.G. Moretto, S. Bradley, W.L. Kehoe, and A.C. Mignerey, Nucl. Phys. **A476**, 516 (1988).

[20] R. Planeta, S.H. Zhou, K. Kwiatkowski, W.G. Wilson, V.E. Viola, H. Breuer, D. Benton, F. Khazaie, R.J. McDonald, A.C. Mignerey, A. Weston-Dawkes, R.T. de Souza, J.R. Huizenga, and W.U. Schröder, Phys. Rev. C **38**, 195 (1988).

[21] S.J. Yennello, B. Young, J. Yee, J.A. Winger, J.S. Winfield, G.D. Westfall, A. Vander Molen, B.M. Sherrill, J. Shea, E. Norbeck, D.J. Morrissey, T. Li, E. Gualtieri, D. Craig, W. Benenson, and D. Bazin, Phys. Lett. B **321**, 15 (1994).

[22] R.J. Charity, Computer code GEMINI. The code is available via anonymous FTP from WUNMR.WUSTL.EDU in directory/pub/gemini.

[23] N.G. Nicolis, D.G. Sarantites, L.G. Sobotka, and R.J. Charity, Phys. Rev. C **45**, 2393 (1992).

[24] C. Wagemans, in *The Nuclear Fission Process*, edited by C. Wagemans (CRC Press, Boca Raton, 1991), p. 545.

[25] W. E. Ormand, P.F. Bortignon, A. Bracco, and R.A. Broglia, Phys. Rev. C **40**, 1510 (1989).

[26] K.T.R. Davies, K.R. Sandhya Devi, and M. R. Strayer, Phys. Rev. C **20**, 1372 (1979).

[27] N. Cârjan, A. Sierk, and J.R. Nix, Nucl. Phys. **A452**, 381 (1986).

[28] W. Bauer, Prog. Part. Nucl. Phys. **30**, 45 (1993).

[29] G. D. Westfall, W. Bauer, D. Craig, M. Cronqvist, E. Gualtieri, S. Hannuschke, D. Klakow, T. Li, T. Reposeur, A.M. Vander Molen, W.K. Wilson, J.S. Winfield, J. Yee, S.J. Yennello, R. Lacey, A. Elmaani, J. Lauret, A. Nadasen, and E. Norbeck, Phys. Rev. Lett. **71**, 1986 (1993).